The Egyptian Journal of Remote Sensing and Space Sciences 27 (2024) 356–368

Contents lists available at ScienceDirect

The Egyptian Journal of Remote Sensing and Space Sciences

journal homepage: www.sciencedirect.com

Research Paper

Implementation of a UAV-aided calibration method for a mobile dual-polarization weather radar

Giorgio Buckingham [a,b], Mario De La Cruz [a,b], Danny Scipion [b], Juan C. Espinoza [b], Joab Apaza [b], Guillermo Kemper [a,*]

[a] Faculty of Engineering, School of Electronic Engineering, Universidad Peruana de Ciencias Aplicadas, Av. Prolongación Primavera 2390, Monterrico, Santiago de Surco, Lima 15023, Peru

[b] Jicamarca Radio Observatory, Instituto Geofísico del Peru, S/N, Lurigancho, Chosica, Lima 15464, Peru

ARTICLE INFO

Keywords:
Weather radar
UAV
Calibration
Reflectivity

ABSTRACT

Weather radar calibration is a crucial factor to be considered for quantitative applications, such as QPE (Quantitative Precipitation Estimation), which is used as input for weather risks management. The present work proposes a novel approach to the end-to-end radar calibration method through the characterization of the radar weighting functions. These are Gaussian functions that model an additional attenuation factor to the radar received power. This approach, based on the inclusion these parameters, allow the obtainment of a calibrated equivalent reflectivity factor expression for a Doppler dual-polarization weather radar that operates in the X band. To calculate these parameters, a UAS (Unmanned Aircraft System) was implemented for suspending the calibration target with a well-defined cross-section and for measuring its inclination due to wind using an IMU (Inertial Measurement Unit). From its measurements, the position of the target can be estimated, which is essential to the characterization of the weighting functions. Their inclusion within the radar equation, alongside the implementation of the angular measurement system highlight the innovation to the traditional radar calibration methodology that does not contemplate them from the explored state-of-the-art. The reflectivity was compared with the measurements from a disdrometer for a moderate rain event. An average reflectivity difference of 0.75 dBZ and a percent bias of 3.3 % were obtained between the expected and estimated measurements when including these functions compared to the 1.51 dBZ and –62.7 % obtained when disregarding them. These experimental results point out that the proposed method can deliver superior accuracy in the reflectivity estimation.

1. Introduction

Radar systems are used in a broad spectrum of applications (Waldschmidt et al., 2017), (Khan and Power, 1995), (National Research Council, 2002). Weather radars play an essential role in meteorological research, which can lead to a better understanding of weather conditions and eventually to the mitigation of several weather hazards through forecasts using data ingested usually from a network of radars (Mamalakis et al., 2020). However, an uncalibrated or poorly calibrated radar is a source of degraded data, which limits the usefulness of the radar and contributes to erroneous and misleading estimates.

Calibrating a weather radar typically involves adjusting the reflectivity factor calibration (Christodoulou et al., 2004). One of the most reliable methods for weather radar calibration involves an end-to-end approach using reference reflectors as passive targets (Suh et al., 2017). To enhance the precision of radar parameters, particularly when the scatterer's location within the radar resolution is uncertain, the radar range and beam weighting functions are integrated into the radar equation. These functions introduce an additional attenuation factor due to the scatterer's position in both angular and range within the resolution volume (Chen et al., 2011). Previous research has primarily focused on evaluating the impact of these range and beam-width weighting functions on radar received power (Scipion et al., 2008). However, there has been a notable lack of research regarding the utilization of these functions in characterizing the radar's hard-targets equation, specifically when the scatterer's position inside the resolution volume is known. Traditionally, the end-to-end method using spherical targets requires the simultaneous use of a weather balloon to suspend the

* Corresponding author.
E-mail address: guillermo.kemper@upc.pe (G. Kemper).

https://doi.org/10.1016/j.ejrs.2024.04.005
Received 24 November 2023; Received in revised form 12 February 2024; Accepted 17 April 2024
Available online 23 April 2024

Table 1
List of similar works related to the weather calibration using UAVs.

Author	Approach	Application	Strengths	Weaknesses
(Duthoit et al., 2017)	Usage of a UAV carrying a gimbal with an RF probe and a foil-wrapped foam sphere.	Antenna characterization, radome inspection and radar calibration using metal sphere.	Standard deviation of 0.35 dB for differential reflectivity obtained for measurements across one experiment.	Calibration only considers the differential reflectivity for a single RHI and disregards the calibration of the reflectivity obtained for a single channel.
(Joshil and Chandrasekar, 2022)	Usage of a UAV suspending a metal sphere.	Calibration of the dual-frequency dual-polarization 3DR weather radar	Reflectivity offsets obtained between 1.33 and 2.21 dBZ for 3 of the 4 receiving channels of the radar.	Only the difference between the expected and measured reflectivity values for the metal sphere was considered for the validation.
(Yin et al., 2019)	Usage of a UAV suspending a GNSS system alongside a metal sphere	Calibration of an S-band mobile Doppler weather radar	Extensive characterization of the antenna. The calculated radar constants have small standard deviations within 1 dB among different experiments.	Calibration in the radar operational mode could not be performed due to legal UAV flying height limitations in the Netherlands.
(Williams et al., 2013)	End-to-end calibration using metal spheres	Differential reflectivity calibration of a NEXRAD weather radar	Difference of 0.2 dB obtained between the theoretical reflectivity and the measured results. Manufactured metal spheres of two different sizes were considered for the analysis.	Only the difference between the expected and measured reflectivity and differential reflectivity values for the metal sphere was considered for the validation.

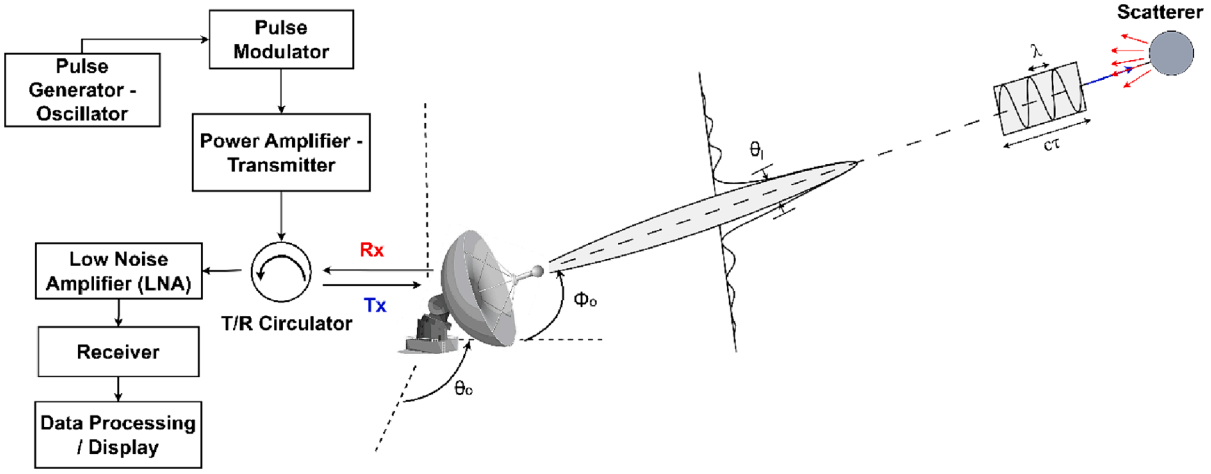

Fig. 1. Block diagram of a pulsed Doppler radar and a representation of the backscattering of the transmitted pulses.

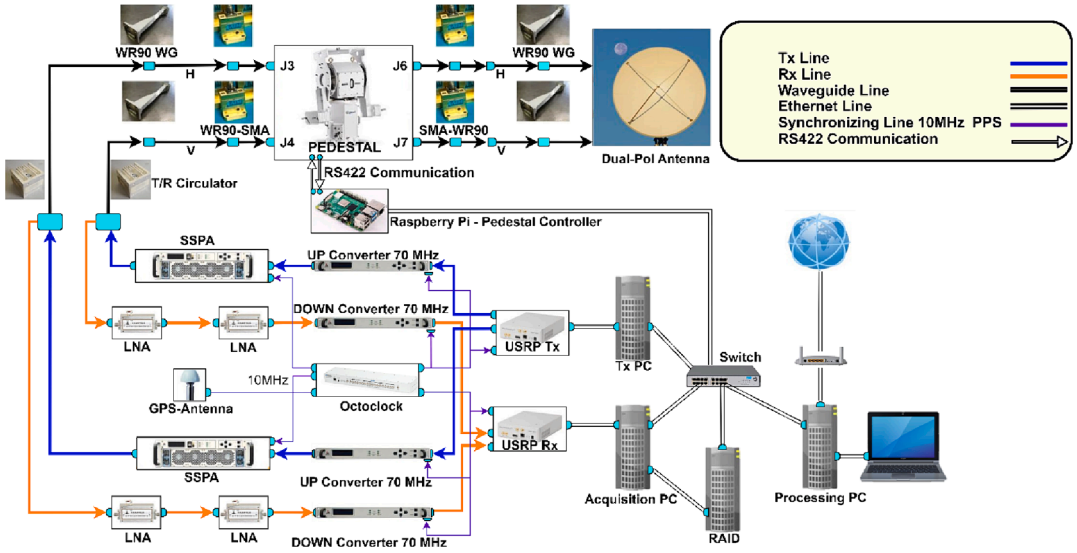

Fig. 2. Diagram of the SOPHy weather radar.

reflector. However, certain conditions and considerations must be taken into account for this method to yield a successful calibration (Manz et al., 2000).

Nowadays, the usage of Unmanned Aerial Vehicles (UAV) has been extended into many applications for remote sensing (Apaza et al., 2017), (Hafeez et al., 2023). Flying targets are a well-documented option for radar calibration, specifically balloon-borne targets, and aircraft. However, these targets are associated with certain drawbacks in operability,

Table 2
Operational parameters of the SOPHy weather radar.

Parameter	Value
Radar type	Dual Polarization / Doppler
Operative frequency	9.345 GHz
Wavelength	0.032 *m*
Radar pointing range	AZ: (0°-360°) – EL: (−5°-185°)
Max. observable range	60 km
Antenna beamwidth	1.8°
Antenna diameter	1.21 *m*
Antenna gain	38.5 dBi
Scanning modes	PPI, RHI, combined
Pulse compression coding schemes	CC8, CC16, CC32, CC64, CC128
Peak transmitting power	Solid state 200 W

cost, and scan strategy flexibility. The usage of UAVs can mitigate many of those drawbacks by selecting a custom remote flying trajectory. However, this method is not exempt of drawbacks, as the pendulum-like motion of the airborne hanging sphere can lead to a significant position uncertainty of the target.

A review of the explored implementations of radar calibration is presented in Table 1; as can be observed, none of the previous works uses the radar range or beam weighting functions in the characterization of the radar equation for point targets. Additionally, none of the explored works uses similar instrumentation for validating the reflectivity measurements obtained using the radar constant. These types of comparisons can lead to standardized radar networks, which is crucial for remote sensing studies.

This work's main contribution is a weather radar calibration method that uses a spherical target to obtain a radar constant that includes the characterization of the radar range and beam weighting function in the radar equation. The described method also includes the implementation of a UAV-based device for measuring the position of the airborne target. This device consists of a System-On-Chip (SoC) unit, an Inertial Measurement Unit (IMU), and several custom-built pieces that allow the integration of the target to the UAV. The reflectivity measurements obtained using the calibration constant were validated using a disdrometer while sampling the same phenomena. For a moderate rain event, an average reflectivity of 0.75 dBZ and a percent bias of 3.3 % was obtained between the expected and estimated measurements while including the weighting functions in the radar constant characterization. When these functions were disregarded, an average reflectivity value of 1.51 dBZ and a percent bias of –62.7 % was obtained. These results show an elevated degree of agreement between instruments which suggest a high precision rate in the reflectivity estimations using the proposed method.

Furthermore, this paper is organized as follows. Section 2.1 provides an overview of weather radars, the weather radar used in this paper and the main equations used for the calibration. Section 2.2 explains the design and development of the aircraft used for the calibration method alongside the planning of the calibration experiments. Section 2.3

Fig. 3. UAS used for the calibration, alongside the spherical target.

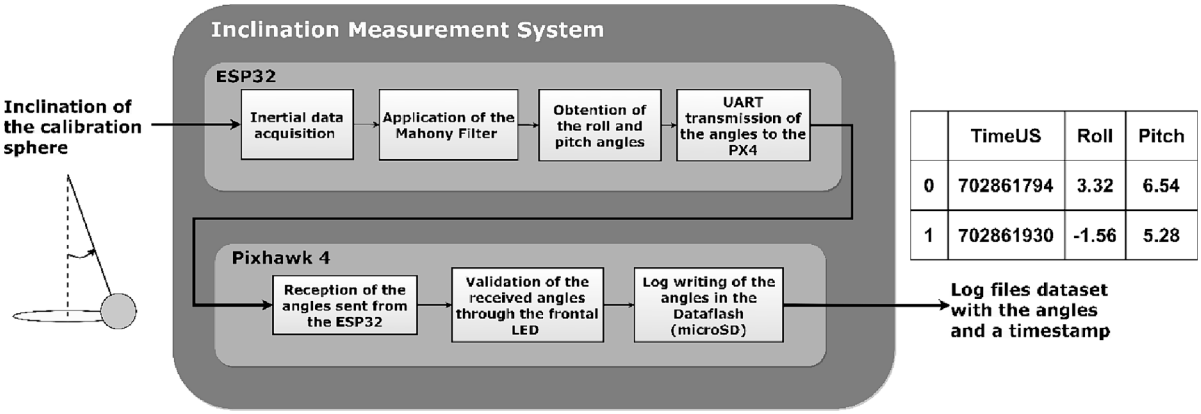

Fig. 4. Calibration system including the UAS coupled to the mechanism that lifts the sphere, the 30 m cable, and the metal sphere.

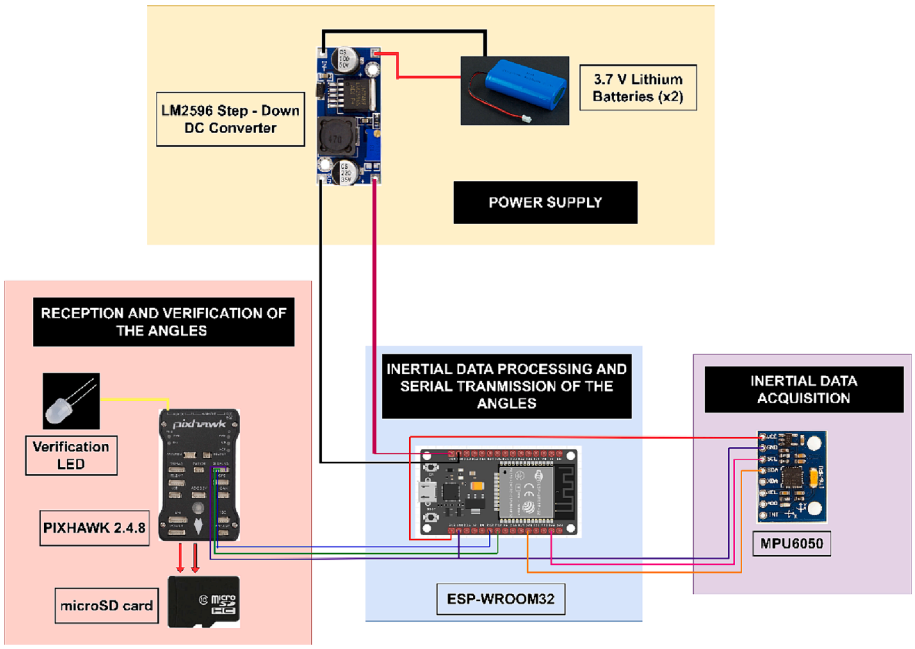

Fig. 5. Diagram of the angular measurement system and its interconnecting interfaces.

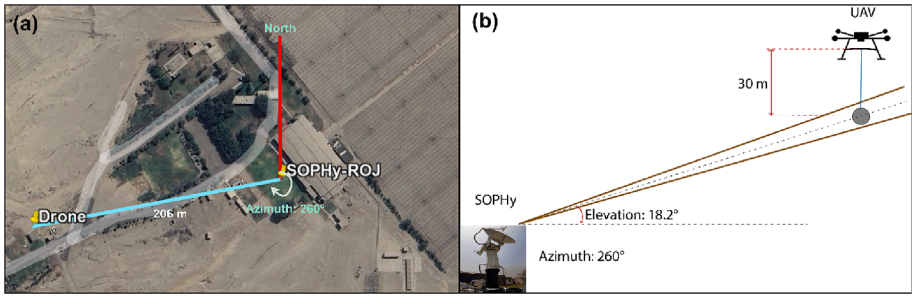

Fig. 6. (a) Top view of the calibration experiment's location (b) Side view of it.

Table 3
Operational parameters of the SOPHy radar used during the calibration experiments at the Jicamarca Radio Observatory.

Parameter	Value
Pedestal Speed	10°/s
Elevation Range	0 – 40°
Azimuth Range	[2° – 4°]
Heading	−26°
Pulse Width	0.1μ s
Sampling Rate	20 MHz
Range Resolution	15 m
Inter-Pulse Period (IPP)	60 km
Mode	RHI

describes the development of the calibration method involving the processing of the data obtained from the experiments and the calculation of the radar calibration constant. Section 3 explains the obtained results alongside the validation using a reference instrument. Finally, major conclusions and contributions are stated in Section 4.

2. Materials and methods

2.1. The Doppler weather radar

2.1.1. Overview

The pulsed Doppler weather radar basic diagram, as depicted in Fig. 1 includes a pulse generator through a local oscillator, a pulse modulator and a power amplifier that introduces a large gain to the pulsed signal before being transmitted through the antenna (Doviak and Zrnić, 1993). A small part of the back-scattered pulses from the targets towards the antenna are filtered and amplified. A circulator is included between the antenna and the transmit/receive devices, which acts as an interface to the RF back-scattered signals and the high-power signals from the transmitter. Before entering the receiver, the amplified pulsed signal is converted from a microwave signal into an intermediate frequency signal. Finally, this signal is processed to obtain the Doppler shift, spectral width and received power, also known as radar moments from its I-Q voltage components. The received power is essential in the radar equation characterization and the reflectivity factor (Z) estimation. One of the main advantages that dual-polarization radars offer is that the moments from each individual polarization can be used to calculate polarimetric variables (Chandrasekar et al., 2013). On a dual-polarization weather radar, the moments from each receiving channel are combined and processed to obtain variables that are used to classify hydrometeors and to perform Quantitative Precipitation Estimation

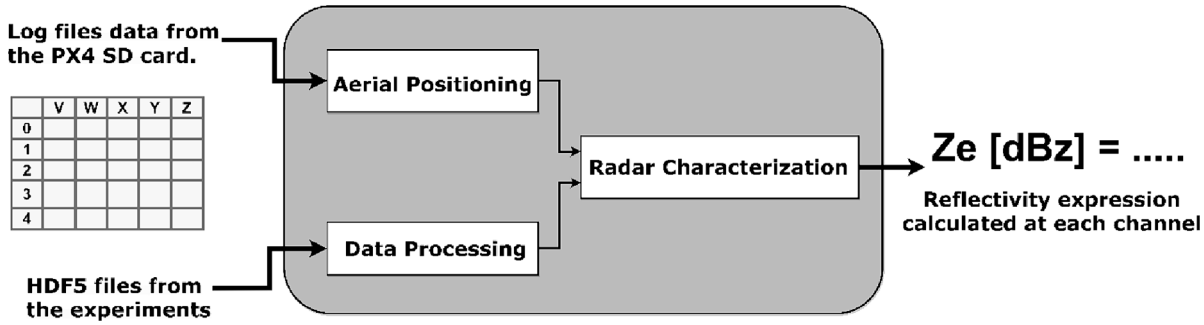

Fig. 7. Block diagram of the radar calibration procedure, including the input data coming from experiment performed and the output as the calibrated reflectivity expression.

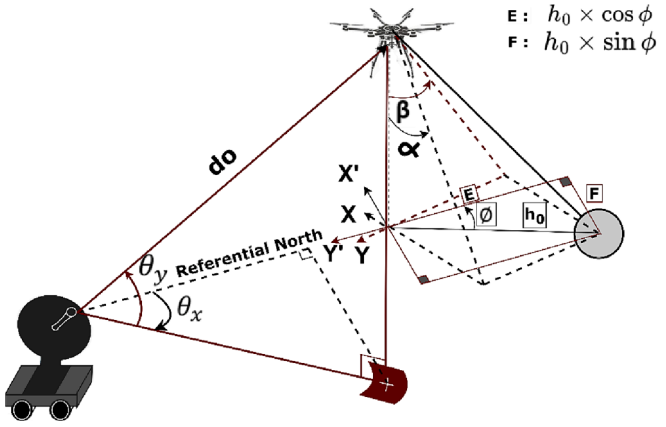

Fig. 8. Geometrical model of the metal sphere position considering the rotation in the Z axis (yaw) of the UAS compared to the reference North, which is also mapped + Y axis of the positioning model, in this case the E and F distances were considered to the model.

(QPE) for approximating the amount of precipitation that has fallen over certain regions (Neuper and Ehret, 2019).

2.1.2. The SOPHy weather radar

The Scanning-system for Observation of Peruvian Hydrometeorological events (SOPHy) (Espinoza et al., 2021) is an innovative mobile weather radar created by the Geophysical Institute of Peru (IGP) at the Jicamarca Radio Observatory. Operating in the X-band at a 9.345 GHz frequency with dual-polarization capabilities, SOPHy is designed to estimate various weather radar variables. These measurements serve the dual purpose of quantifying precipitation levels and classifying the presence of hydrometeors in the Peruvian atmosphere. SOPHy's transmission and reception system is based on Software Defined Radio (SDR), enabling the flexibility to test different waveforms for transmitting pulses and reconfigure receiving parameters through software. The radar system offers versatile scanning capabilities with two modes: Plan Position Indicator (PPI) and Range Height Indicator (RHI), achieved through azimuth or elevation movements of the radar pedestal. Fig. 2 provides a pictorial diagram of SOPHy's radar system, encompassing both transmitting and receiving modes, along with each polarization. Table 2 presents the key operational parameters for the SOPHy radar.

2.1.3. The radar equation

The hard-targets radar equation (Skolnik, 1980), which relates the

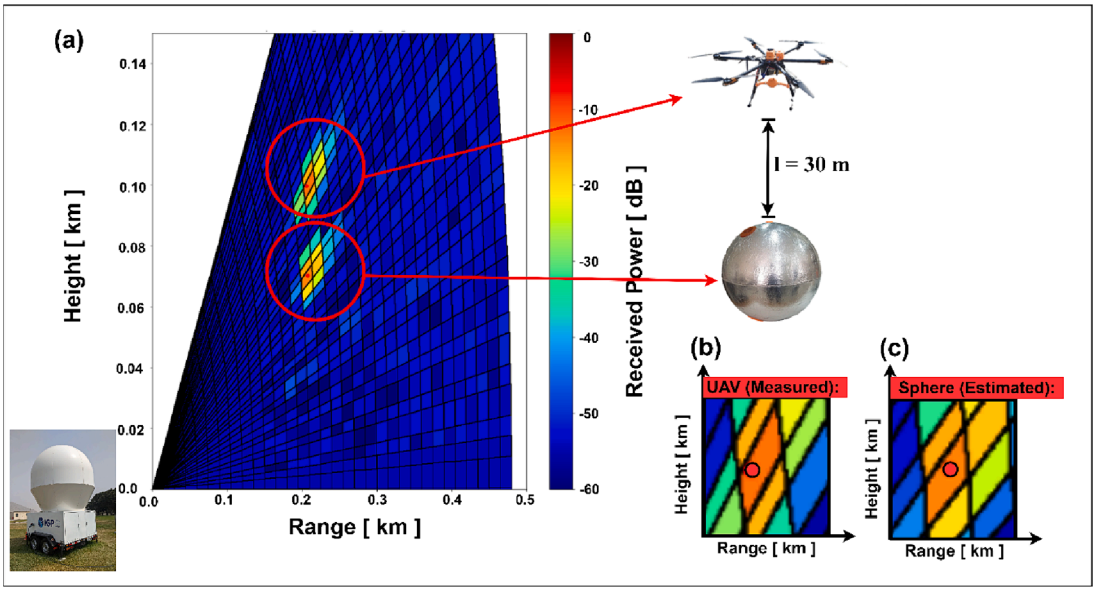

Fig. 9. (a) S-H plot for one of the samples from experiment 2, showing the signatures for the UAV and the sphere. (b) Position of the UAV measured using its GPS coordinates. (c) Estimated position of the metal sphere using the angular measurement system within its resolution volume.

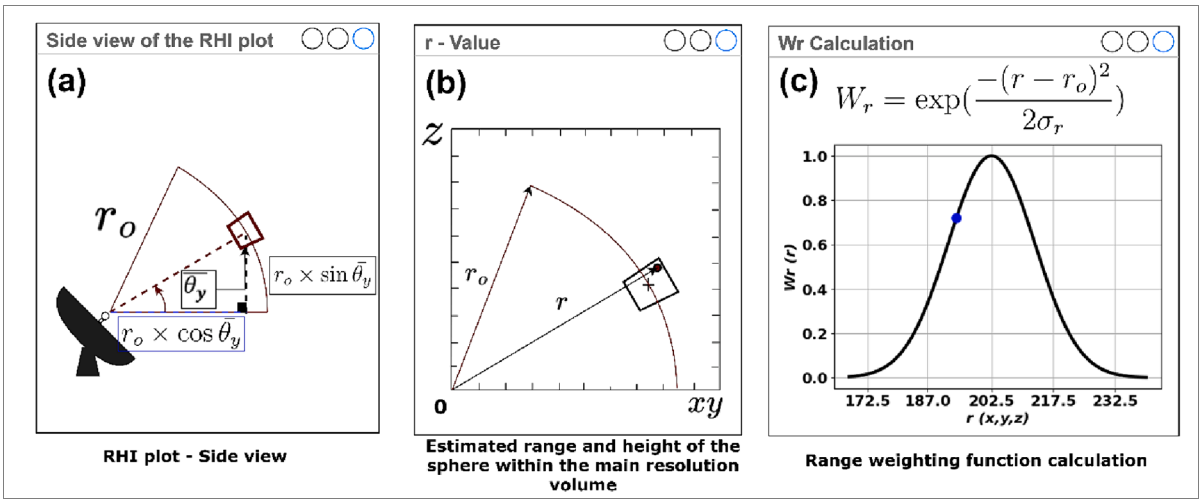

Fig. 10. Range weighting function calculation from the distance in range estimated for the sphere. (a) Side view, where the distance to the center of the volume resolution r_0 is shown. (b) Addition of the estimated distance in range of the sphere r. (c) Range weighting function W_r plotted.

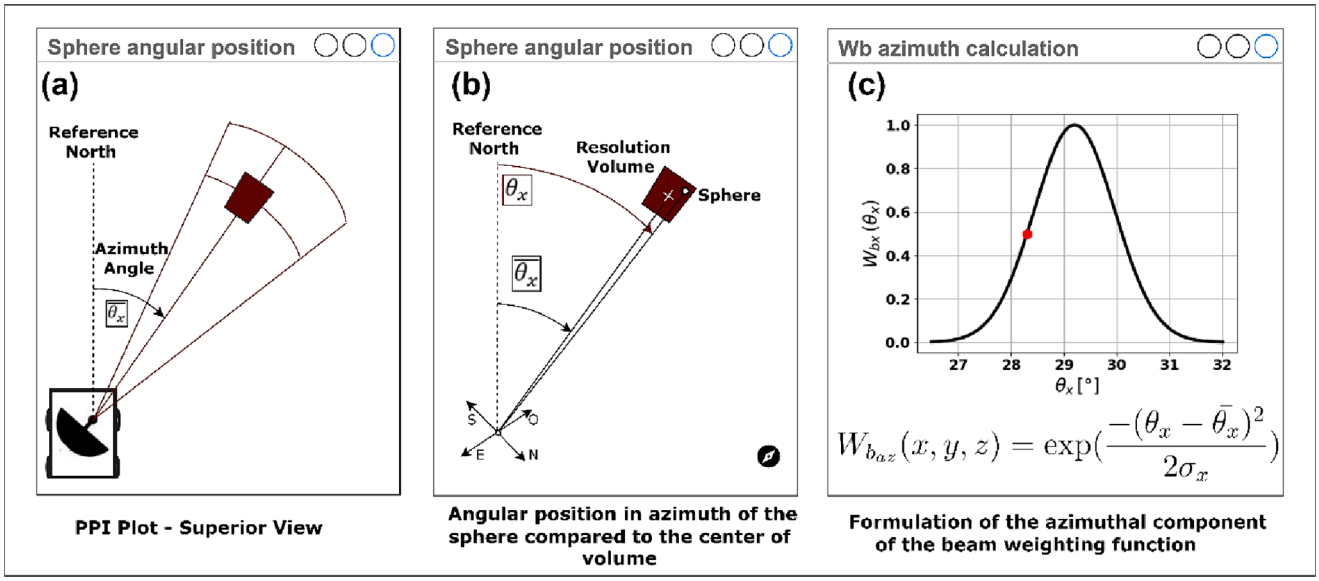

Fig. 11. Azimuth component of the beam weighting function calculation using the estimated angular position of the sphere and the beam. (a) Visualization of the angular position in azimuth of the center of the radar beam $(\bar{\theta}_x)$ using the North as reference. (b) Addition of the estimated angular position in azimuth of the sphere. (θ_x). (c) Azimuthal component of the beam weighting function (W_{b_x}).

power of the back-scattered echoes measured at the receiver of the radar to several of its operational parameters was slightly modified to perform a more in-depth characterization of the SOPHy radar,

$$P_r = \frac{P_t G^2 G_{LNA} \lambda^2}{(4\pi)^3 r^4 L^2} \sigma W_r W_b, \tag{1}$$

where P_t and P_r are the radar transmitting power and receiving power, respectively; G is the gain of the antenna; λ is the operational wavelength, σ is the radar cross-section of the scatterer, r is the distance in range from the center of the antenna to the target and L^2 is the unknown variable related to all the external and internal losses of the system. Additionally G_{LNA} is the total gain from the low noise amplifiers at the receiver and W_r and W_b are the range and beam weighting functions, these are Gaussian functions that model the received power distribution due to the angular position and range of the scatterer within a single resolution volume (Holdsworth and Reid, 1995), (Yu, 2000), (Cheong et al., 2004). From this equation, the fixed parameters and the losses variable can be grouped at the left side into a hard-targets calibration constant C_{sph} (Eq. (2), leaving the variable parameters at the right side of the expression:

$$C_{sph} = \frac{P_r r^4}{P_t \sigma_{sph} G_{LNA} W_r W_b} \tag{2}$$

For calculating an equivalent reflectivity expression, the previously estimated constant can be plugged in alongside other additional fixed parameters from the soft-targets equation. to calculate a soft-targets constant C_z (Eq. (3), where c is the speed of light, τ is the width of the transmitted pulses, θ_l is the effective beam-width of the antenna of the radar in radians and K_m is the complex dielectric constant associated to the distributed target, in this case water. Finally, an equivalent radar reflectivity expression Z_e is calculated using the previous soft-targets constant and the variable radar parameters in Eq. (4).

$$C_z = \frac{16 ln 2 \lambda^4}{C_{sph} c \theta_l^2 \pi^6 |K_m|^2} \times 10^{18} \tag{3}$$

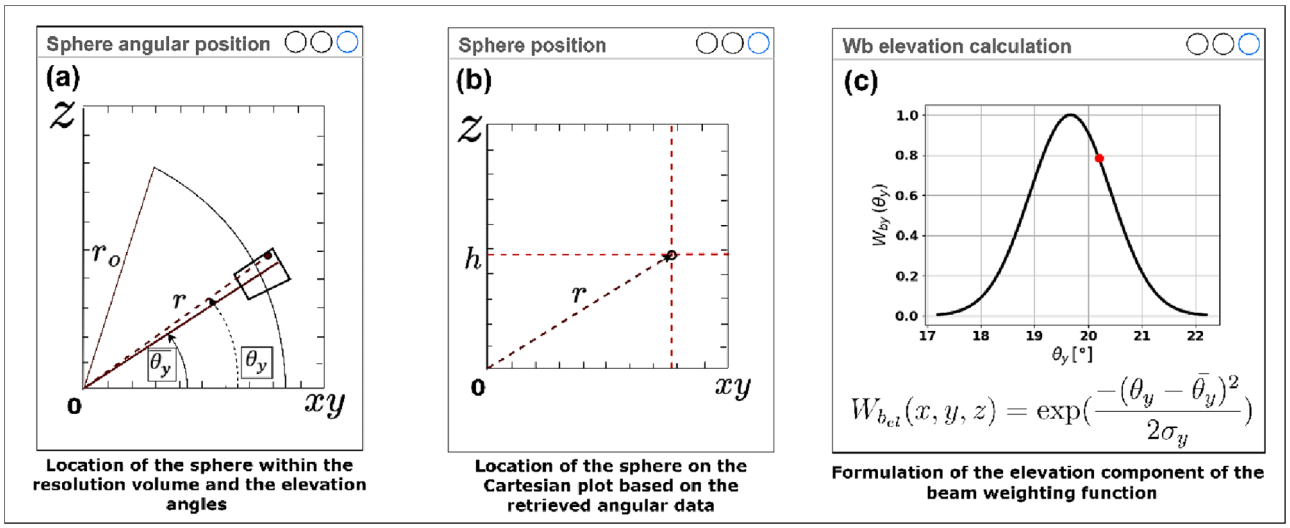

Fig. 12. Elevation component of the beam weighting function calculation using the estimated angular position of the sphere and the beam. (a) Visualization of the angular position in elevation of the center of the radar beam $(\overline{\theta_y})$. (b) Addition of the estimated angular position in elevation of the sphere. (θ_y). (c) Elevation component of the beam weighting function. $\left(W_{b_y}\right)$

Table 4
Status of the calibration experiments performed.

Experiment	Tx Mode	Status	Observations
1	Horizontal	Usable	Low quantity of samples
2	Vertical	Usable	None
3	Vertical	Usable	None
4	Vertical	Not Usable	Incorrect measurements from the inclination system.
5	Horizontal	Usable	None
6	Horizontal	Not Usable	Failed to save the received data from the correct channel.

$$Z_e\left[mm^6m^{-3}\right] = \frac{P_r r_o^2 C_z}{P_t \tau G_{LNA}} \tag{4}$$

2.2. Design and implementation of the calibration method

The proposed calibration method adopts the widely used end-to-end radar calibration technique employing metal spheres (Li et al., 2016). The choice of a spherical target is deliberate, as it provides a constant and precisely defined cross-section relative to the radar's pulse wavelength. To facilitate the calibration process, an Unmanned Aerial System (UAS) was deployed to suspend the target during calibration experiments. Furthermore, an angular measurement system was integrated into the UAS to measure the cable inclination caused by wind.

2.2.1. Implementation of the UAS as a calibration target

The UAV employed for suspending the calibration target is built around a foldable carbon fiber Tarot T960 mm frame. The onboard flight controller is the 3DR Pixhawk board (Dronecode Foundation, 2020), an open-source system, using the Copter firmware from Ardupilot (Ardupilot, 2023). To build the hexacopter into a calibration target, an additional structure for lifting the sphere was affixed to the UAV, positioned between the hexacopter's legs. This structure features a rolling mechanism to properly hoist the metal sphere. The spherical target itself consists of a 0.35 m diameter Styrofoam sphere covered with aluminum foil. At the upper pole of the sphere, there is a small aperture where a 30-meter metal rope attaches to lift and suspend the sphere in the air. This separation allows for the distinct recognition of two radar echoes to distinguish the UAV from the sphere. Characterizing the spherical target in the radar equation involves calculating its radar cross-section, which belongs to the optical region. In this region, the cross-section depends solely on the sphere's circumference, πr^2, where r represents the radius of the spherical scatterer (Fukao and Hamazu, 2013). The optical region can be guaranteed with the following expression:

$$\frac{2\pi a}{\lambda} \geq 12 \tag{5}$$

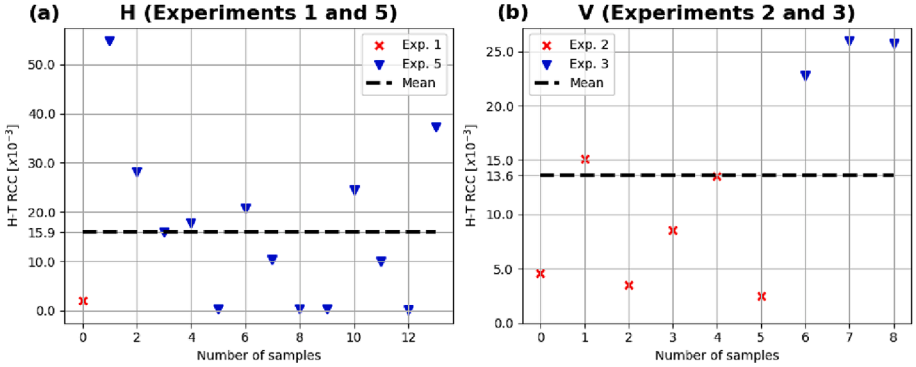

Fig. 13. Hard targets constant values $((\times 10^{-3}))$ across the samples when (a) using the samples gathered from the experiments using the horizontal polarization mode. (b) using the samples gathered from the experiments using the vertical polarization mode.

Table 5
Comparison of the different radar calibration constant values obtained across all the calibration experiments.

Scenario	Hard-targets constant ($\times 10^{-3}$)		Soft-targets constant [dB]		
	H	V	H	V	| H –V |
Using the weighting functions in the radar characterization	15.9	13.6	63.58	64.26	0.67
Disregarding the weighting functions in the radar characterization	9.46	9.05	65.84	66.03	0.19

where a is the radius of the sphere and λ is the operational wavelength of the SOPHy radar. Using this expression, the minimum radius of the sphere needed to locate the sphere in the optical region is 0.063 m. The UAS, including the UAV, the metal sphere with its 30 m length cable, and the structures coupled to main structure is displayed on Fig. 3.

2.2.2. Development of the angular measurement system

To quantify the radar range and beam weighting functions, the following steps were determined:

Step 1: Implement a mechanism that measures the tilt of the cable connected to the UAV and allows the calibration sphere to be suspended freely rotating on 3 axes. Since the sphere is prone to move from its rest position due to external factors (i.e. wind). Fig. 4 shows the block diagram of the tilt measurement system.

Step 2: An inclination measurement system was developed and placed into a small structure next to the flight controller of the UAV (Apfata et al., 2021) For acquisition and processing use an inertial measurement system (IMU) MPU6050 (Alzamora et al., 2022) and a System-On-Chip Espressif ESP-WROOM32 development board adapted on the UAV. Also, the quaternion algorithm (Kim and Golnaraghi, 2004) and the Mahony filter algorithm (Mahony et al., 2008) were used in the processing to solve the attitude fusion. From the obtained quaternions, the Euler roll and pitch angles were retrieved and sent to the Pixhawk Serial4 interface. A diagram of the proposed device is shown in Fig. 5.

Step 3: For storage of the obtained data the Ardupilot firmware installed on the Pixhawk was modified to include receiving the angles and writing them to the flight logs in an external flash memory along with a timestamp provided by a GPS. To verify the correct reception and writing of the angles, a notifier LED connected to one of Pixhawk's auxiliary ports was installed.

Step 4: Finally, the sphere was positioned within the radar resolution volume in a Cartesian model to characterize the beam weighting functions in the radar equation for hard targets, since these functions depend on the position of the scatterer.

2.2.3. Experiment setup

To perform the calibration experiments with the SOPHy radar, its distance to the UAS had to be set from a minimal value calculated by the radar far field, which is the region where the resultant field of the antenna pattern can interfere constructively into an evenly wave front (Haridimm et al., 2016). With a regular parabolic antenna, the far field region can be calculated with the following expression (from SOPHy's parabolic antenna dish parameters):

$$r_{far}[m] = \frac{2D^2}{\lambda} \tag{6}$$

where $D = 1.21$ m and $\lambda = 0.032$ m (see Table 1). With these values the far field was estimated to start at 92.6 m. Considering this, the distance from the radar to location of the UAS was set to 200 m (Fig. 6a). From a side-view (Fig. 6b), the UAS was located 100 m above the ground in a loiter mode maintaining a fixed location, heading, and altitude. This mode allows the stabilization of the sphere in a fixed spot neglecting the wind effects.

Six calibration experiments were performed from May 7th to May 9th, 2022. Table 3 displays the scanning pattern and the radar parameters set for the experiments.

2.3. Radar calibration procedure

The radar calibration block diagram is depicted in Fig. 7. This includes the radar data processing step, a step related to the aerial positioning that was elaborated to obtain the Cartesian coordinates of the sphere from the roll and pitch angles and the GPS coordinates of the UAV of the inclination measurement system, and the characterization of the radar equation using all the parameters collected from the experiments performed to obtain a calibrated equivalent reflectivity expression.

2.3.1. Aerial positioning system

To characterize the radar weighting functions, the aerial positioning of the calibration sphere was performed using the retrieved inclination angles associated to the 30-meters cable from the UAS controller flight logs. The following steps briefly explain the algorithms that transform those inclination angles into a referential sphere position.

Step 1: The positioning of the Unmanned Aerial System (UAS) was accomplished through a Geodesic to Cartesian transformation (Burtch, 2006), using GPS coordinates for both the SOPHy radar's location and the UAS, taking the former as the reference point.

Step 2: The positioning of the sphere relative to the UAS was deter-

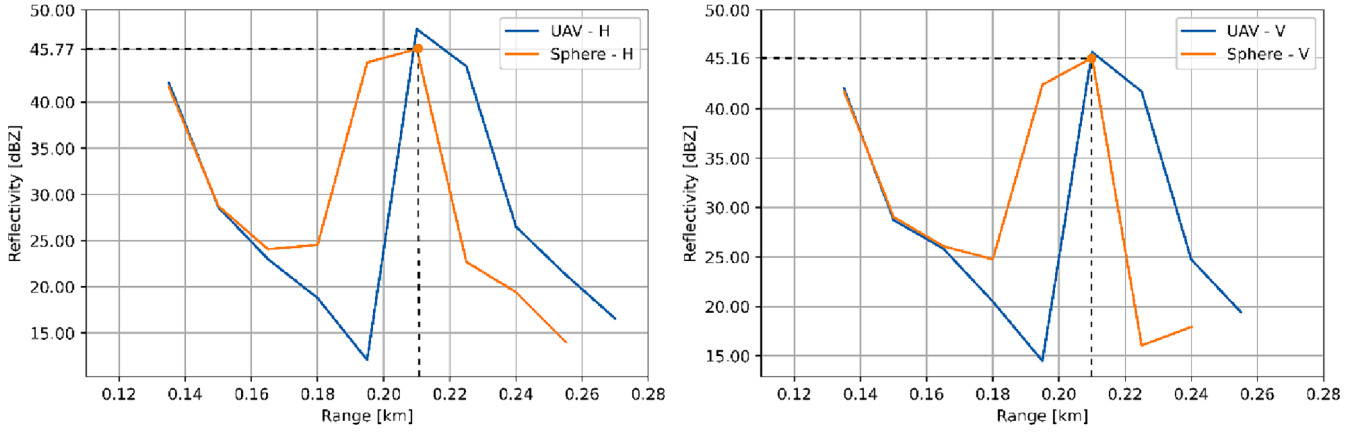

Fig. 14. Range profiles with the average reflectivity values across all the maximum echoes from the UAS and sphere signature from each RHI including all the calibration experiments for each polarization mode.

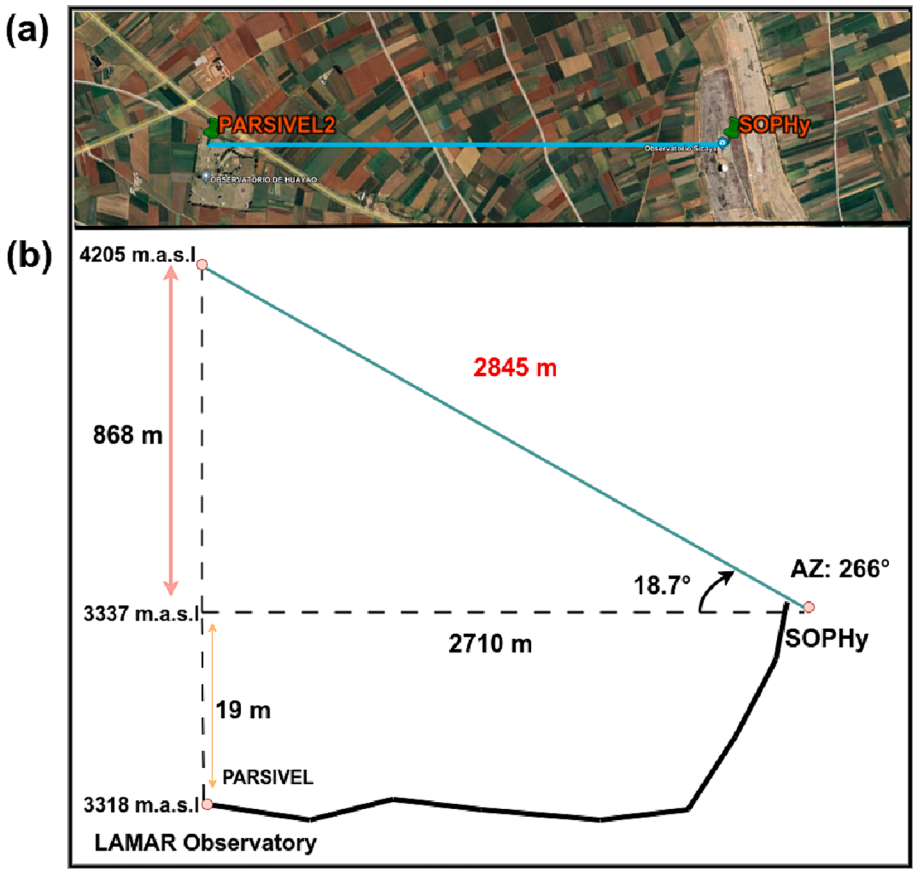

Fig. 15. (a) Location of the SOPHy radar and the PARSIVEL^2 disdrometer installed on the LAMAR observatory. (b) Side view of the SOPHy radar pointing above the LAMAR observatory alongside the distances between the instruments.

mined using the equivalence of roll and pitch angles in Euler coordinates to the first two angles in spherical coordinates. Using the range distance (d_o) from SOPHy to the UAS, along with the roll (α) and pitch (β) angles, the distances in the Cartesian model were calculated, estimating the distance from the sphere's resting position to its current location on the same XY plane (h_0).

Step 3: The yaw offset (ϕ) was incorporated into the model to compensate the rotation of the UAS. This approach enabled the calculation of E and F perpendicular distances aligned with the + X and + Y axes (Fig. 8).

Step 4: Finally, considering the 30-meter vertical length of the cable from the UAS in its resting position, the sphere's Cartesian coordinates were determined concerning the SOPHy radar.

2.3.2. Radar data processing step

The processing of the radar data collected from the calibration experiments is described in the following steps:

Step 1: Using the RHI files for all the samples retrieved from the calibration experiments, the power signatures associated to the UAV and the sphere were plotted alongside the estimated positions of the UAV in a "S-H" plot (Fig. 9). This "S-H" scale considers the curvature of the Earth to the range and height calculations. This plot was done to validate the estimations of the sphere using the positioning model.

Step 2: To calculate the range weighting function values, from the processed radar data, the estimated range of the sphere (r), and the distance in range to the center of the resolution volume that contains the sphere (r_o) were included in Eq. (4), alongside the variance associated to the transmitted pulse for the experiment. On Fig. 10, the procedure is explained, showing the distances including the plot of the range weighting function for the resolution volume that contains the sphere.

Step 3: To estimate the azimuth component of the beam weighting function, the azimuth angle that goes from the reference North to the location of the sphere (θ_x), a small geometrical model was used (Fig. 11). The azimuth angle of the center of the resolution volume ($\overline{\theta_x}$) was retrieved from the collected radar data associated to the pedestal.

Step 4: For the elevation component of the beam weighting function (Fig. 12), the elevation angle to the center of the beam was compared to the elevation angle associated to the sphere, which was calculated using the estimations of the range and height of the sphere.

Step 5: Finally, with the characterization of each component of the beam weighting function, these now can be evaluated.

3. Results and discussion

Of the six calibration experiments performed, only four of them were considered for analysis. Unfortunately, as only one transmitter was available during the time when the calibration experiments were performed, the differential reflectivity analysis will not be possible to evaluate, as it requires both co-polar channels simultaneously operative. However, in compensation the analysis will be focused on the obtention of the radar constants for the horizontal channel, which leads to a particular reflectivity expression for the SOPHy radar, detailed in Section 3.1. Section 3.2 offers an in-depth comparation of the reflectivity values obtained with the radar constant during a rain event against similar instrumentation, and the impact of the radar weighting functions on this reflectivity estimations. Table 4 summarizes the status and a description for each performed experiment. All the usable samples depending on the co-polar line (horizontal or vertical) connected to the only available transmitter were separated in two different data pools. However, for the calibration constant and reflectivity analysis only the results from the experiments associated to the horizontal channel (1 and 5) were considered.

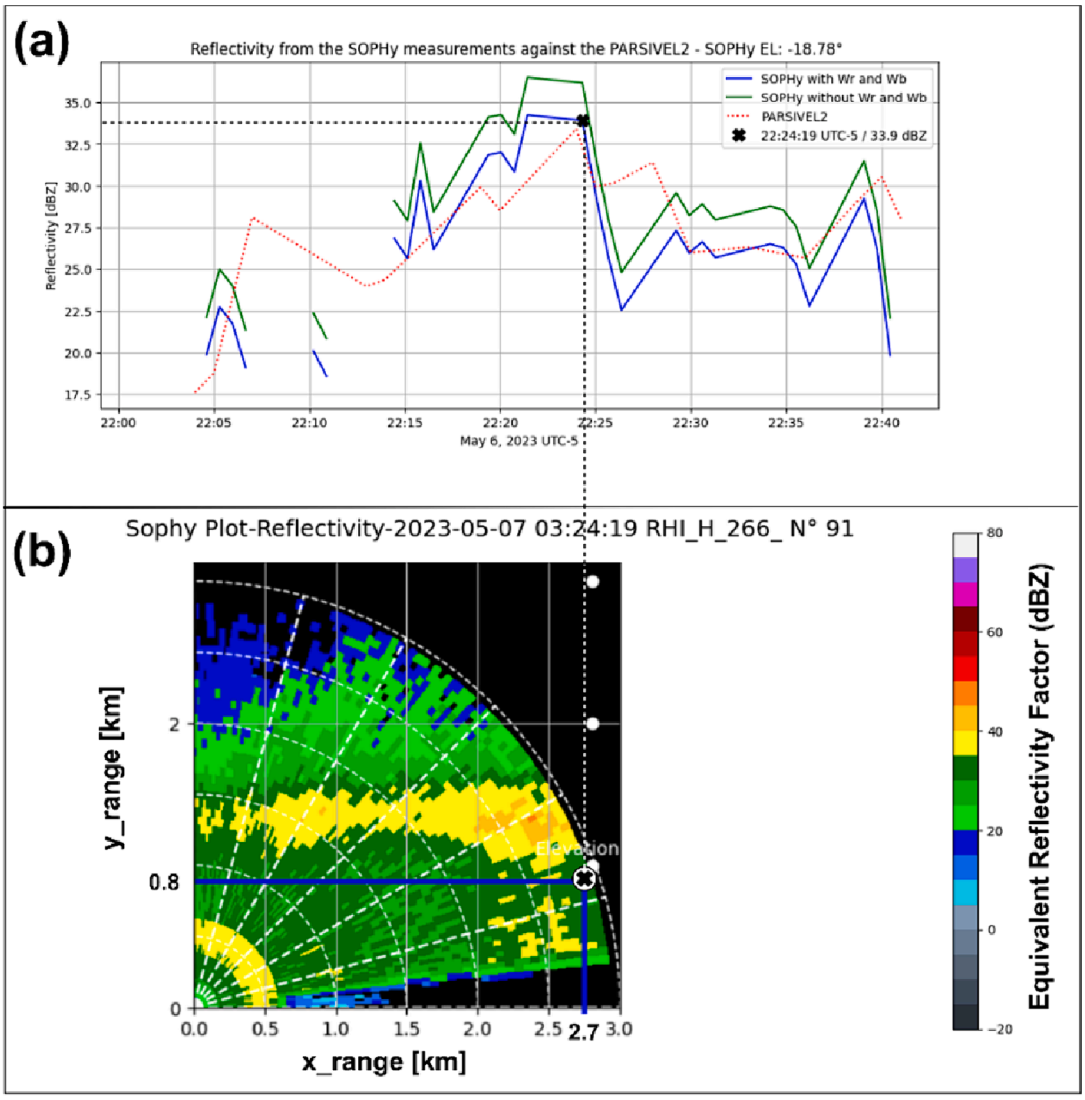

Fig. 16. Rain event captured on May 6th, 2023. (a) Comparison of reflectivity measured by SOPHy against the PARSIVEL^2 at 18.78° el / 266° a. (b) RHI plot for 22:24:19, highlighting a reference echo on a range-height scale.

3.1. Analysis and evaluation of the radar calibration constant values

From the collected data, an average hard-targets constant value was calculated, as it is depicted on Fig. 13 for each different polarization mode used. Table 5 highlights the values of the averaged hard-targets constant values obtained and its soft-targets constant value associated alongside the difference between the horizontal and vertical constant in two different scenarios. The first scenario considers the inclusion of the radar weighting function in the radar hard-targets and soft-targets calculation, while the second excludes them from the radar equation characterization. From this comparison, a difference of 0.67 dB was found between the polarization modes for the first scenario. This value can be interpreted as a difference of the total gains and losses within the characterization of the transmitting and receiving path when using the transmitting line associated to the horizontal or vertical channel. From the comparison between both scenarios, it can be observed that the inclusion of the weighting functions is related to an increment of the hard-targets constant for both channels and a decrement of the soft-targets constant at the same time. A difference of 2.17 dB for the soft-targets constant was obtained comparing both scenarios, which will be analyzed during radar normal operation for comparing the impact of these functions for its reflectivity estimation. The average reflectivity value associated to the UAS and the sphere signatures for each polarization mode used are shown on Fig. 14. This displays the average reflectivity values for the range profile associated to the maximum received power echo obtained for the UAS and the sphere. As it can be observed, average sphere reflectivity values of 45.77 and 45.16 dBZ were obtained for each polarization mode used for across calibration experiments. However, the difference between these values cannot be considered for a differential reflectivity analysis, as each co-polar channel was tested independently and not simultaneously due the absence of a second transmitter for the SOPHy radar during the calibration experiments.

3.2. Validation of the calibration during operation

To analyze the performance of the calibration constant for the SOPHy radar a comparison of the reflectivity values was performed using reference instrumentation. This comparison was performed pointing towards the Atmospheric Microphysics and Radiation Laboratory (LAMAR) (Flores-Rojas et al., 2021), located in the Junín region of Peru at the Huancayo Observatory at 3 km from the Sicaya Observatory where SOPHy is currently installed. The PARSIVEL^2 (Particle Size and Velocity) is an optical disdrometer that measures both the size and speed

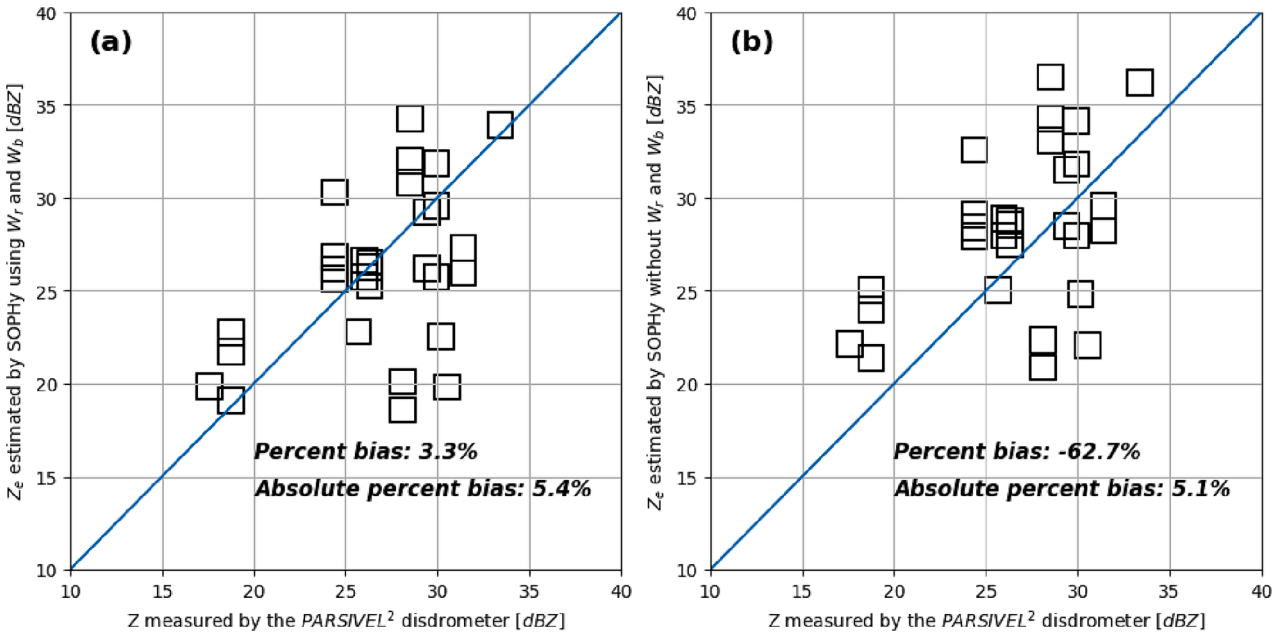

Fig. 17. (a) Correlation chart between the SOPHy reflectivity estimations and the PARSIVEL^2 disdrometer measurements using the radar weighting functions to calculate the radar constant. **(b)** Correlation chart without using the radar weighting functions to calculate the radar constant.

Table 6
Comparison between the expected and the estimated results for the May 6th, 2023 rain event.

Scenario	Average expected Reflectivity (PARSIVEL^2) (dBz)	Average estimated Equivalent Reflectivity (SOPHy) (dBz)	| Average Expected Reflectivity – Average Estimated Reflectivity | (dBZ)
Using the weighting functions in the radar characterization	26.74	25.98	0.75
Disregarding the weighting functions in the radar characterization	26.74	28.24	1.51

of small falling particles to calculate the reflectivity associated with the precipitation that falls across its laser beam (Löffler-Mang and Joss, 2000). The geographical location of both instruments is shown on Fig. 15.

For a May 6th, 2023, rain event, Fig. 16a. highlights the comparison between the reflectivity measured by SOPHy against the PARSIVEL^2 pointing above the LAMAR observatory across a 40-minute interval for both soft-targets constant obtained from Table 5. A reflectivity sample for the 10:24 PM time was selected to showcase the RHI plot associated with this sample (Fig. 16b). The chosen echo from Fig. 15a can be observed here at a range of 2.7 km and a height of 800 m, which is associated to the 33.9 dB equivalent reflectivity factor value.

To compare the event rain totals between both instruments, the percent bias and percent absolute bias metrics were used, which are calculated for n samples as:

$$Percentbias = \frac{\sum_{i=1}^{n}(x_i - y_i)}{\sum_{i=1}^{n} x_i} \times 100\%, \tag{7}$$

$$Percentabsolutebias = \frac{\sum_{i=1}^{n}|x_i - y_i|}{\sum_{i=1}^{n} x_i} \times 100\%, \tag{8}$$

where x is the reference instrument variable (reflectivity measured by the PARSIVEL^2) and y the variable to compare against it (reflectivity measured by the SOPHy radar). These biases were considered as it is a direct comparison between instrumentation that measure or estimates the same variable.

The correlation between the reflectivity estimations of SOPHy and the PARSIVEL^2 was calculated for the two cases from Table 5 (Fig. 17). For the first scenario, a percent bias between instruments of 3.3 % and an absolute percent bias of 5.4 % was found compared to the –62.7 % and 5.1 % for the second scenario. From the correlation charts, the second scenario exhibits a vertical shift of 2.17 dBZ compared to the first due to the increment of the soft-targets constant. The results obtained for the first scenario indicate an elevated level of agreement between instruments, which suggest that the inclusion of the radar weighting functions in the radar constant characterization can lead to more accurate reflectivity estimations.

Optical disdrometers such as the PARSIVEL^2 can be a valid reference for multi-dimensional weather instrumentation calibration on light to moderate rain events without hail (Kalina et al., 2014). The expected and estimated reflectivity values for the captured rain event are summarized in Table 6. As can be observed, the SOPHy horizontal polarization estimations have a 0.75 dBZ difference compared to the PARSIVEL^2 measurements for the first scenario, in contrast to the 1.51 dBZ for the second case, demonstrating encouraging results. However, the low quantity of collected data and the reflectivity discrepancies for heavy rainfall and hail events incites further analysis.

4. Conclusions

This work introduced a novel weather radar calibration method for the SOPHy radar, incorporating radar range and beam weighting functions into the radar equation. By characterizing these functions and indirectly estimating parameters that are challenging to model separately, this unique approach was employed to calibrate the horizontal co-polar channel of the SOPHy radar. To facilitate the characterization, a UAS was utilized to suspend the calibration sphere and measure its

inclination in the presence of wind. The calibration also involved incorporating the hard-targets constant into the radar soft-targets equation, yielding a calibrated equivalent reflectivity (Z_e) expression.

During a moderate rain event, the comparison with a PARSIVEL^2 disdrometer showed a 3.3 % bias when considering radar weighting functions, compared to −62.7 % when disregarding them, demonstrating significant agreement between instruments when weighting functions were included. This suggests that the inclusion of the weighting functions in the radar equation can reduce the uncertainty rate in the reflectivity estimations, which also leads to improvement of the detection rate for a weather radar. However, the limited operational data pool emphasizes the need for further validations with a larger data source.

Future work can explore the calibration of differential reflectivity (Z_{DR}), as this is one of the main factors leading to the correct classification between different hydrometeors. For this work, the horizontal and vertical polarization of the SOPHy radar were not simultaneously operational during the calibration experiments. One of the main challenges that a co-polar calibration supposes is the identification of a similar noise figure between each radar receiver, as this heavily relies on the optimal state of the multiple devices included on a single polarization line. Finally, a multi-instrumental comparation is encouraged for the validation of the reflectivity values obtained across multiple rainfall events.

5. Declarations

The authors would like to thank the Dirección de Investigacion of Universidad Peruana de Ciencias Aplicadas for funding and logistical support with code UPC-D-102–2022 and the Jicamarca Radio Observatory – Geophysical Institute of Peru for technical and economic support. The Jicamarca Radio Observatory is a facility of the Geophysical Institute of Peru operated with support from NSF AGS-2213849 through Cornell University.

6. Validation data

The authors also would like to thank project" TAMYA – Impactos de la precipitación, registrados con un radar meteorológico, en los cuerpos glaciares Andinos: nevado Huaytapallana," through agreement 082–2021-FONDECYT for the data used during the validation process.

Declaration of Competing Interest

The authors declare that they have no known competing financial interests or personal relationships that could have appeared to influence the work reported in this paper.

References

Alzamora, L., Espino, J., Acosta, R., Marquez, M., Kemper, G., 2022. An electronic equipment for monitoring, detection and warning of pitch motion of vehicle drivers. International Conference on Applied Technologies (ICAT) 2022, vol. 1756, 261-263, https://doi.org/10.1007/978-3-031-24971-6_19.

Apaza, J., Scipion, D., Lume, D., Saito, C., 2017. Development of two UAVs for volcano studies in southern Peru. IEEE XXIV International Conference on Electronics, Electrical Engineering and Computing (INTERCON), 1–4, https://doi.org/10.1109/INTERCON.2017.8079700.

Apfata, N., Castillo, J.E., Kemper, G., 2021. Equipo para la deteccion de extraccion de sangre en pacientes, con capacidad de registro de datos temporales y monitoreo de llenado del tubo de venopunción. (Peru Patent No. 2021-2145) Indecopi. https://patentscope.wipo.int/search/en/detail.jsf?docId=PE344435488.

ArduPilot, 2023. Introducing copter. Available online at: https://ardupilot.org/copter/docs/introduction.html, last accessed on 22.06.2023.

Burtch, R.C., 2006. A Comparison of Methods Used in Rectangular to Geodetic Coordinate Transformations. ACSM Annual Conference and Technology Exhibition.

Chandrasekar, V., Beauchamp, R., Bechini, R., 2023. Introduction to Dual Polarization Weather Radar. Cambridge University Press. https://doi.org/10.1017/9781108772266.

Chen, J., Chen, C., Furumoto, J., 2011. Radar beam- and range-weighting effects on three-dimensional radar imaging for the atmosphere. Radio Sci. 46, 6014. https://doi.org/10.1029/2011RS004715.

Cheong, B.L., Hoffman, M., Palmer, R., 2004. Efficient atmospheric simulation for high-resolution radar imaging applications. Journal of Atmospheric and Oceanic Technology 21. https://doi.org/10.1175/1520-0426(2004)021<0374:EASFHR>2.0.CO;2.

Christodoulou, C.I., Michaelides, S.C., Gabella, M, Pattichis, C.S., 2004. Prediction of rainfall rate based on weather radar measurements. IEEE International Joint Conference on Neural Networks (IEEE Cat. No.04CH37541), https://doi.org/10.1109/IJCNN.2004.1380153.

Doviak, R., Zrnić, D., 1993. Doppler Radar and Weather Observations," (2nd edition), San Diego: Academic Press, doi: https://doi.org/10.1016/C2009-0-22358-0.

Duthoit, S., Salazar, J.L., Doyle, W., Segales, A., Wolf, B., Fulton, C., Chilson, P., 2017. A new approach for in-situ antenna characterization, radome inspection and radar calibration, using an unmanned aircraft system (UAS). 2017 IEEE Radar Conference (RadarConf), https://doi.org/10.1109/RADAR.2017.7944287.

Espinoza, J.C., Scipion, D., Valdez, A., Verastegui, J., 2021. SOPHy: Scanning-system for observations of Peruvian hydrometeorological-events. IEEE International Conference on Aerospace and Signal Processing (INCAS). https://doi.org/10.1109/INCAS53599.2021.9666928.

Flores-Rojas, J.L., Silva, Y., Suárez-Salas, L., Estevan, R., Valdivia-Prado, J., Saavedra, M., Giraldez, L., Piñas-Laura, M., Scipión, D., Milla, M., Kumar, S., Martinez-Castro, D., 2021. Analysis of Extreme Meteorological Events in the Central Andes of Peru Using a Set of Specialized Instruments. Atmosphere MDPI AG 12 (3), 408. https://doi.org/10.3390/atmos12030408.

Dronecode Foundation, 2020. Pixhawk 1 Flight Controller. Available online at: https://docs.px4.io/v1.9.0/en/flight_controller/pixhawk.html, last accessed on 21.09.2023.

Fukao, S., Hamazu, K., 2013. Radar for Meteorological and Atmospheric Observations. Springer Japan. https://doi.org/10.1007/978-4-431-54334-3.

Hafeez, A., Husain, M., Singh, S.P., Chauhan, A., Khan, M., Kumar, N., Chauhan, A., Soni, S.K., 2023. Implementation of drone technology for farm monitoring & pesticide spraying: A review. Information Processing in Agriculture 10 (2), 192–203. https://doi.org/10.1016/j.inpa.2022.02.002.

Haridim, M., Tsaliovich, A., Gavan, J., Razban, T., 2016. Radiating antenna near/far field distribution and region boundaries. 2016 IEEE Conference on Antenna Measurements & Applications (CAMA), https://doi.org/10.1109/CAMA.2016.7815748.

Holdsworth, D., Reid, I., 1995. A simple model of atmospheric radar backscatter: Description and application to the full correlation analysis of spaced antenna data. Radio Sci. 30, 1263–1280. https://doi.org/10.1029/95rs00645.

Joshil, S., Chandrasekar, C.V., 2022. Calibration of D3R weather radar using UAV-hosted target. Remote Sens. (basel) 14 (15), 3534. https://doi.org/10.3390/rs14153534.

Kalina, E.A., Friedrich, K., Ellis, S.M., Burgess, D.W., 2014. Comparison of Disdrometer and X-Band Mobile Radar Observations in Convective Precipitation. Mon. Weather Rev. 142 (7), 2414–2435. American Meteorological Society, https://doi: 10.1175/mwr-d-14-00039.

Khan, R.H., Power, D., 1995. Aircraft detection and tracking with high frequency radar. Proceedings International Radar Conference. https://doi.org/10.1109/RADAR.1995.522517.

Kim, A., Golnaraghi, M.F., 2004. A Quaternion-Based Orientation Estimation Algorithm Using an Inertial Measurement Unit. IEEE Position Location and Navigation Symposium 268–272. https://doi.org/10.1109/PLANS.2004.1309003.

Li, Z., Chen, H., Duan, S., Bi, Y., Lei, H., Lai, Y., Wu, H., Li, D., 2016. Reflectivity calibration for X-band solid-state radar with metal sphere. IEEE International Geoscience and Remote Sensing Symposium (IGARSS). https://doi.org/10.1109/igarss.2016.7730243.

Löffler-Mang, M., Joss, J., 2000. An optical disdrometer for measuring size and velocity of hydrometeors. J. Atmos. Oceanic Tech. 17, 130–139. https://doi.org/10.1175/1520-0426(2000)017.

Mahony, R., Hamel, T., Pflimlin, J., 2008. Nonlinear complementary filters on the special orthogonal group. IEEE Trans. Automat. Contr. 53 (5), 1203–1218. https://doi.org/10.1109/TAC.2008.923738.

Mamalakis, A., Ebert-Uphoff, I., Barnes, E.A., 2020. Explainable artificial intelligence in meteorology and climate science: Model fine-tuning, calibrating trust and learning new science. xxAI - Beyond Explainable AI, ser. Springer International Publishing, pp. 315–339.

Manz, A., Smith, A.H., Hardaker, P.J., 2000. Comparison of different methods of end-to-end calibration of the U.K. weather radar network. Physics Chem. Earth: b: Hydrol. Oceans Atmosphere 25 (10–12), 1157–1162. https://doi.org/10.1016/S1464-1909(00)00171-4.

National Research Council, 2002. Weather Radar Technology Beyond NEXRAD. The National Academies Press, Https://. https://doi.org/10.17226/10394.

Neuper, M., Ehret, U., 2019. Quantitative precipitation estimation with weather radar using a data- and information-based approach. Hydrol. Earth Syst. Sci. 23 (9), 3711. https://doi.org/10.5194/hess-2018-606.

Scipion, D., Chilson, P., Fedorovich, E., Palmer, R.D., 2008. Evaluation of an LES-based wind profiler simulator for observations of a day-time atmospheric convective boundary layer. J. Atmos. Ocean. Technol. 25 (8), 1423. https://doi.org/10.1175/2007JTECHA970.1.

Skolnik, M., 1980. 1980. McGraw-Hill, Introduction to Radar Systems. ser. Electrical Engineering Series.

Suh, J., Minz, L., Jung, D., Kang, H., Ham, J., Park, S., 2017. Drone-based external calibration of a fully synchronized Ku-band heterodyne FMCW radar. IEEE Trans. Instrum. Meas. 66 (8), 2189–2197. https://doi.org/10.1109/TIM.2017.2687518.

Waldschmidt, C., Hugler, P., Geiger, M., 2017. Radar as an emerging and growing technology for industrial applications: A short overview. Proceedings Sensor 2017, AMA. https://doi.org/10.5162/sensor2017/D3.1.

Williams, E., Cho, J., Smalley, D., Sandifer, J., Zrnic, D., Melnikov, V., Burgess, D., Forsyth, D., Webster, T., Erickson, D., 2013. End-to-end calibration of NEXRAD differential reflectivity with metal spheres. 36th Conference on Radar Meteorology. American Meteorological Society.

Yin, J., Hoogeboom, P., Unal, C., Russchenberg, H., Van der Zwan, F., Oudejans, E., 2019. UAV-Aided weather radar calibration. IEEE Trans. Geosci. Remote Sens. 57 (12), 10362–10375. https://doi.org/10.1109/TGRS.2019.2933912.

Yu, T., 2000, Radar studies of the atmosphere using spatial and frequency diversity.